Rare Met.
https://doi.org/10.1007/s12598-024-02906-3

RARE METALS

ORIGINAL ARTICLE

$WSe_2/MoSe_2$ with a better-matched heterointerface dominating high-performance potassium/sodium storage

Zhi-Yuan Song, Yun-Dong Cao, Lin-Lin Fan*, Jian Song, Yi Feng*, Hong Liu, Cai-Li Lv, Guang-Gang Gao*

Received: 11 January 2024 / Revised: 1 May 2024 / Accepted: 7 May 2024

Abstract Constructing a valid heterointerface with a built-in electric field is an effective strategy for designing energy storage anodes with exceptional efficiency for potassium-ion batteries (PIBs) and sodium-ion batteries (SIBs). In this study, $WSe_2/MoSe_2$ nanosheets with a better-matched and stable heterojunction interface were uniformly embedded in carbon nanofiber frameworks ($WSe_2/MoSe_2$/CNFs). The ion/electron transfer kinetics were facilitated by heterointerfaces with an enlarged effective utilization range. Meanwhile, the heterointerface directed electron transfer from $MoSe_2$ to WSe_2 and had significant potassium adsorption capability. The ultra-high pseudocapacitance contribution originating from the heterostructure and morphological features of the $WSe_2/MoSe_2$ nanosheets contributed to enhancing high-rate energy storage. Moreover, in situ X-ray diffraction and ex situ X-ray photoelectron spectroscopy revealed the potassification/depotassification behavior of the $WSe_2/MoSe_2$/CNFs during the conversion reaction. Consequently, after 500 cycles at 5 $A{\cdot}g^{-1}$, the $WSe_2/MoSe_2$/CNF anode demonstrated an outstanding long-term cycling performance of 125.6 $mAh{\cdot}g^{-1}$ for PIBs. While serving as a SIB electrode, it exhibited an exceptional rate capability of 243.5 $mAh{\cdot}g^{-1}$ at 20 $A{\cdot}g^{-1}$. With the goal of developing high-performance PIB/SIB electrode materials, the proposed strategy, based on heterointerface adaptation engineering, is promising.

Keywords Heterointerface; Metal selenides; Potassium-ion batteries; Sodium-ion batteries; High-rate capability

1 Introduction

Exploiting environmentally safe and high-performance electrical energy storage devices is vital, given the continuous consumption of traditional fossil fuels and severe environmental pollution. The energy storage industry has seen growth in the utilization of lithium-ion batteries (LIBs) mainly owing to their exceptional cycle stability and high energy density [1]. Nevertheless, the use of LIBs in large-scale storage systems has been limited by the poor specific capacity of graphite electrodes as well as the scarcity and high cost of lithium [2]. Because of the abundant natural resources and the low redox potential of K and Na (− 2.92 V (vs. K/K^+) and − 2.71 V (vs. Na/Na^+)), electrochemical potassium-ion batteries (PIBs) and sodium-ion batteries (SIBs) are attracting considerable attention and demonstrating a vast commercialization potential for low-cost and large-scale energy storage systems [3–6]. Notably, the large radius and weight of K^+/Na^+ result in a massive diffusion barrier, slow reaction kinetics, and poor power density, which adversely affect rate capability and cycle life [7]. Therefore, designing effective electrode materials with high comprehensive performance for PIBs/SIBs is imperative.

Supplementary Information The online version contains supplementary material available at https://doi.org/10.1007/s12598-024-02906-3.

Z.-Y. Song, Y.-D. Cao, L.-L. Fan*, J. Song, Y. Feng*, H. Liu, C.-L. Lv, G.-G. Gao*
Collaborative Innovation Center of Metal Nanoclusters and Photo/Electro-Catalysis and Sensing, School of Materials Science and Engineering, University of Jinan, Jinan 250022, China
e-mail: mse_fanll@ujn.edu.cn

Y. Feng
e-mail: mse_fengy@ujn.edu.cn

G.-G. Gao
e-mail: mse_gaogg@ujn.edu.cn

Published online: 24 July 2024

It is recognized that a heterostructure that combines the advanced functions and strengths of multiple materials has the synergistic effect of employing the benefits of each individual component while avoiding their drawbacks to accomplish the impact of $1 + 1 > 2$ [8]. Charge transfer and adsorption are facilitated by built-in electric fields generated at the interface owing to the potential difference between the two materials in the heterostructure [9]. Meanwhile, a remarkable number of heterointerface defects and lattice mismatches offer an essential effect on maximizing electrochemical performance [10]. In particular, the heterojunction interface provides a large number of active sites and cause increased ionic diffusion and a maximum charge storage capability to accelerate the storage performance of K^+/Na^+ with a large radius [11, 12]. Additionally, heterostructures exhibit structural stability, which is beneficial for alleviating volume expansion and enhancing cycle life. In the past several years, heterostructure engineering has been reported as a novel and beneficial technique, and studies have confirmed that using the same metal or different metal elements can allow for the construction of heterojunction interfaces that improve the energy storage performance, such as SnS/SnO_2 [13], Co_3O_4/TiO_2 [14], CuS/FeS_2 [15], and WSe_2/NiSe [16]. Notably, studies have tended to neglect the issue of the effective contact area at the heterojunction interface, and only the effective contact region can afford a built-in electric field to facilitate the rapid flow of electrons or ions, which is the most important factor affecting electrochemical performance enhancement. Therefore, optimization of the heterostructure with a better-matched heterointerface is essential for enlarging the interfacial contact area and expanding the range of built-in electric fields.

Transition-metal chalcogenides (TMCs) have garnered considerable attention as potential electrode materials for PIBs/SIBs because of their large interlamellar spacing, high theoretical capacity, and excellent redox reversibility [17, 18]. Among multitudinous TMCs materials, metal selenides, having appropriate working potentials, narrow bandgaps, and high electrical conductivities, are conducive to potassium/sodium storage. Moreover, they have weaker metal–selenium bond energies, which is kinetically favorable for K^+/Na^+ intercalation and deintercalation [19, 20]. As a characteristic layered metal selenide, $MoSe_2$ has been widely employed as PIB/SIB electrode material by right of an intrinsically higher theoretical capacity (422 $mAh{\cdot}g^{-1}$) in a four-electron reaction [21]. The transition metals, such as W and Mo, are homologous elements. When building a heterostructure using WSe_2 and $MoSe_2$, they can be well matched because of their similar space groups ($P6_3/mmc$) and almost equal lattice spacings [22, 23], offering a better option for constructing heterojunction systems with more stable structures and larger effective contact areas. Furthermore, the large interlamellar space (0.65 nm) in WSe_2 and $MoSe_2$ allows for an abundance of large K^+ or Na^+, and the weak van der Waals interactions enhance the reversibility of the electrochemical reaction [24, 25]. Of note, utilization of $WSe_2/MoSe_2$ heterojunctions for sodium or potassium storage has not been reported.

In this study, $WSe_2/MoSe_2$ nanosheets with heterostructures were uniformly embedded in carbon nanofiber frameworks ($WSe_2/MoSe_2$/CNFs) via a straightforward electrospinning technique combined with an in situ selenization procedure. The one-dimensional (1D) nanofibers could shorten the diffusion pathways of ions and enhance the electrical conductivity of anodes. $WSe_2/MoSe_2$ nanosheets with large specific surface areas alleviated the notable volume expansion that occurred during cycling and ensured that K^+/Na^+ was rapidly stored. More importantly, the constructed heterointerface possessed a large charge transport driving force due to the formation of built-in electric fields owing to $WSe_2/MoSe_2$ with a better-matched and stable heterojunction interface, and it offered abundant active sites to accelerate K^+/Na^+ migration. Benefiting from these advantages, the $WSe_2/MoSe_2$/CNF composite displayed excellent cycling behavior and high-rate ability in PIBs and SIBs. After 500 cycles at 5 $A{\cdot}g^{-1}$ for PIBs, it delivered a high reversible capacity of 125.6 $mAh{\cdot}g^{-1}$. For PIBs and SIBs, it was sustained at 133.4 $mAh{\cdot}g^{-1}$ and 243.5 $mAh{\cdot}g^{-1}$, respectively, at a high current density of 20 $A{\cdot}g^{-1}$.

2 Experimental

Phosphotungstic acid (PW_{12}; 0.23 mmol) and phosphomolybdic acid (PMo_{12}; 0.23 mmol) were dissolved in 10 mL of N,N-dimethyl formamide (DMF). Thereafter, 1.5 g of polyvinylpyrrolidone (PVP) was added to the solution, which was then stirred for 12 h. The obtained solution was transferred to a 5-mL syringe, and electrospinning was performed at 50 °C. The distance between the collection device and the needle was 30 cm. A voltage of 19 kV was applied, and the solution supply speed was controlled at 0.03 $mm{\cdot}min^{-1}$. After pre-oxidation at 280 °C for 2 h, the obtained fibers and Se powders (1:3 by mass) were heated at 900 °C under N_2 to synthesize $WSe_2/MoSe_2$/CNFs. The WSe_2/CNFs and $MoSe_2$/CNFs were prepared using similar methods without PMo_{12} and PW_{12}, respectively. Detailed material characterizations, density functional theory (DFT) calculations, and electrochemical measurements are described in Supporting Information.

3 Results and discussion

Figure 1 shows the synthesis pathway used for the $WSe_2/MoSe_2$/CNF composites. First, homogeneous precursor

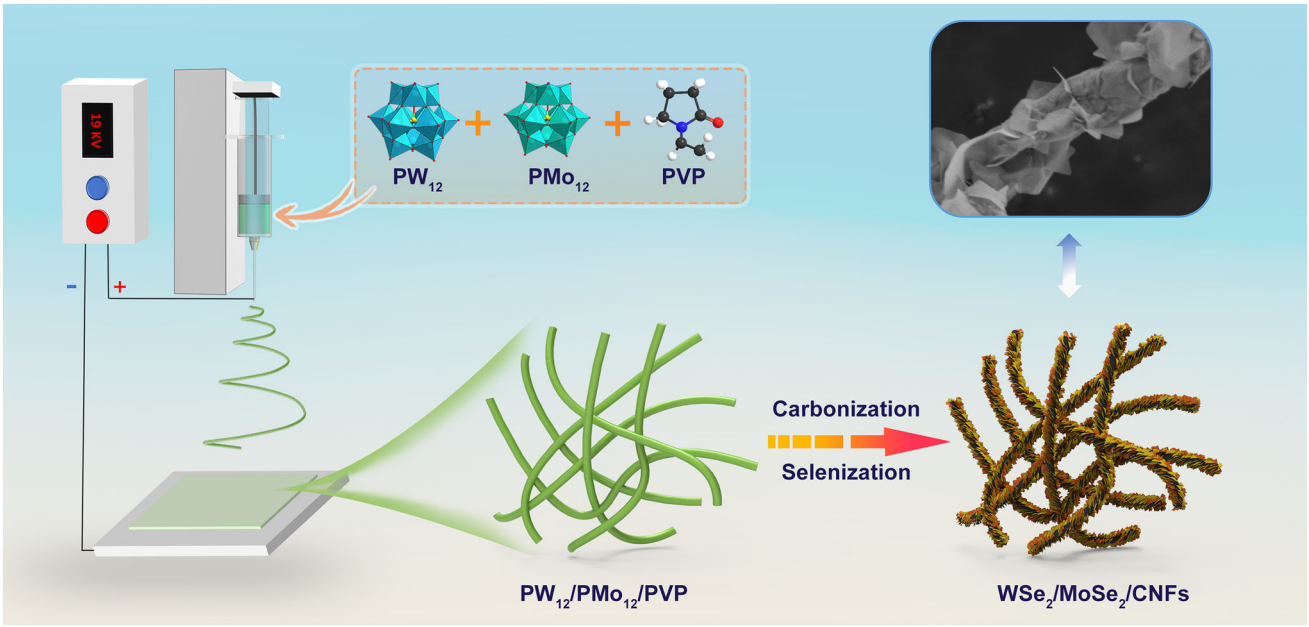

Fig. 1 Schematic synthesis of $WSe_2/MoSe_2$/CNFs composites

solutions were prepared by mixing PW_{12}, PMo_{12}, and PVP with DMF. Electrospinning was performed to obtain PW_{12}/PMo_{12}/PVP. The $WSe_2/MoSe_2$/CNF composites were then formed by carbonization and selenization of the resulting PW_{12}/PMo_{12}/PVP fibers in an N_2 atmosphere. When exposed to high temperatures, PVP transformed into a fibrous carbon substrate, and $WSe_2/MoSe_2$ nanosheets with heterointerfaces were generated on the surface of the CNFs. Scanning electron microscopy and transmission electron microscopy (TEM) were used to characterize the internal structure and surface morphology of the materials. The smooth surfaces of PW_{12}/PMo_{12}/PVP fibers with diameters of 200–300 nm are shown in Fig. S1. Luxuriant $WSe_2/MoSe_2$ nanosheets formed on the surface of the CNFs, forming a unique hierarchical heterostructure (Fig. 2a, b). Similarly, the TEM image shows that the surface of the fibers exhibited a distinct wrinkled and sheet-like structure (Fig. 2c). Figure S2 shows the (002) crystal planes of WSe_2 and $MoSe_2$ according to the high-resolution TEM (HRTEM) images [26, 27]. By contrast, Fig. 2d presents the enlarged interlayer spacing of 0.667 nm, which can be attributed to the (002) heterogeneous interface composed of WSe_2 and $MoSe_2$. Furthermore, as shown in Fig. 2e, the magnified images in Regions I and II reveal the significant alternating distribution of WSe_2 and $MoSe_2$ crystal planes, and the atomic arrangement of the (002) crystal plane illustrates the interfacial atom configuration [28]. These results suggest the distinct two-phase heterointerface of WSe_2 and $MoSe_2$ in the bulk material. Moreover, WSe_2 and $MoSe_2$ exhibit the same hexagonal symmetry with a (002) lattice mismatch of approximately 0.46% (Table S1), which provides an ideal heterostructure for energy storage. C, W, Mo, and Se in the $WSe_2/MoSe_2$/CNF composites were evenly distributed, according to energy-dispersive spectroscopy (EDS) mapping images (Fig. 2f). Figure S3 shows the morphologies of WSe_2/CNFs and $MoSe_2$/CNFs.

X-ray diffraction (XRD) patterns were used to identify the phase components of the as-prepared samples, as shown in Fig. 2g. Without any impurity phases, all characteristic peaks matched well with those of hexagonal $MoSe_2$ (PDF No. 29–0914) and WSe_2 (PDF No. 38–1388) [29, 30]. X-ray photoelectron spectroscopy (XPS) measurements were used to determine the electronic states and surface chemical environments of all three samples. In Fig. 2h, for the W 4f spectrum of the $WSe_2/MoSe_2$/CNFs, W $4f_{7/2}$ and W $4f_{5/2}$ are the two characteristic peaks at 32.4 and 34.5 eV, respectively [31]. Notably, the binding energies shifted slightly to values lower than those of the WSe_2/CNFs. For the Mo 3d spectrum of the $WSe_2/MoSe_2$/CNFs (Fig. 2i), the peaks at 229.0 and 232.1 eV represented Mo $3d_{5/2}$ and Mo $3d_{3/2}$, respectively [32]. The positions of the peaks shifted toward higher binding energies compared with those of the $MoSe_2$/CNFs. These binding energy shifts were attributed to heterophase boundaries, indicating the successful preparation of the $WSe_2/MoSe_2$ heterostructure [33]. Meanwhile, the electron shift from $MoSe_2$ to WSe_2 led to the redistribution of interfacial electrons. The existence of a heterointerface contributed to enhancing K^+/Na^+ mobility and electrochemical reaction kinetics. The peaks at 54.6 and 55.5 eV were well matched to Se $3d_{5/2}$ and Se $3d_{3/2}$ (Fig. 2j),

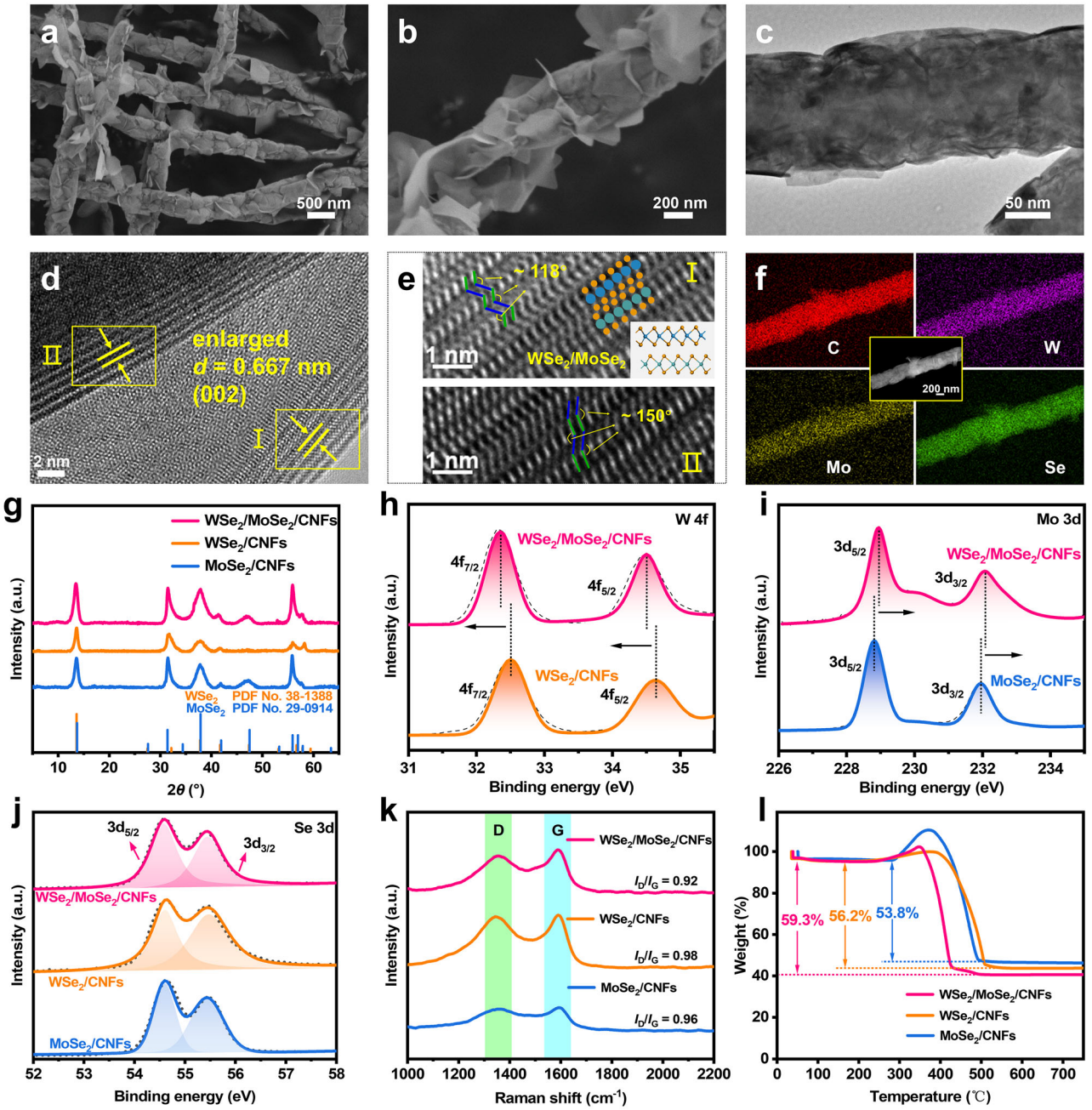

Fig. 2 **a**, **b** SEM images of $WSe_2/MoSe_2$/CNFs; **c–e** TEM and HRTEM images of $WSe_2/MoSe_2$/CNFs; **f** SEM image and corresponding EDS mapping of $WSe_2/MoSe_2$/CNFs; **g** XRD patterns of $WSe_2/MoSe_2$/CNFs, WSe_2/CNFs, and $MoSe_2$/CNFs; **h** W 4f, **i** Mo 3d, and **j** Se 3d XPS spectra for as-prepared samples; **k** Raman spectra and **l** TG analysis curves of three samples

respectively, suggesting a successful selenization reaction [34]. In the Raman spectra (Fig. 2k), the D peak at 1358 cm^{-1} and the G peak at 1586 cm^{-1} corresponded to amorphous carbon and graphitic carbon, respectively. The graphitization degree was evaluated using the I_D/I_G ratio, which reflects the conductivity of composites [35]. The $WSe_2/MoSe_2$/CNFs, WSe_2/CNFs, and $MoSe_2$/CNFs displayed I_D/I_G values of 0.92, 0.98, and 0.96, respectively, indicating their superior electrical conductivity. Notably, the $WSe_2/MoSe_2$/CNFs included specific quantities of carbon defects, which provided appropriate active sites for moving ions and electrons. The thermal properties of the three samples were characterized using thermogravimetric analysis performed in air (Fig. 2l). The early stage of the thermogravimetric analysis was prone to a weight increase, which may have been related to the solid WO_3, MoO_3, and SeO_2 formation [36, 37]. The weight percentages of carbon in $MoSe_2$/CNFs, WSe_2/CNFs, and $WSe_2/MoSe_2$/CNFs

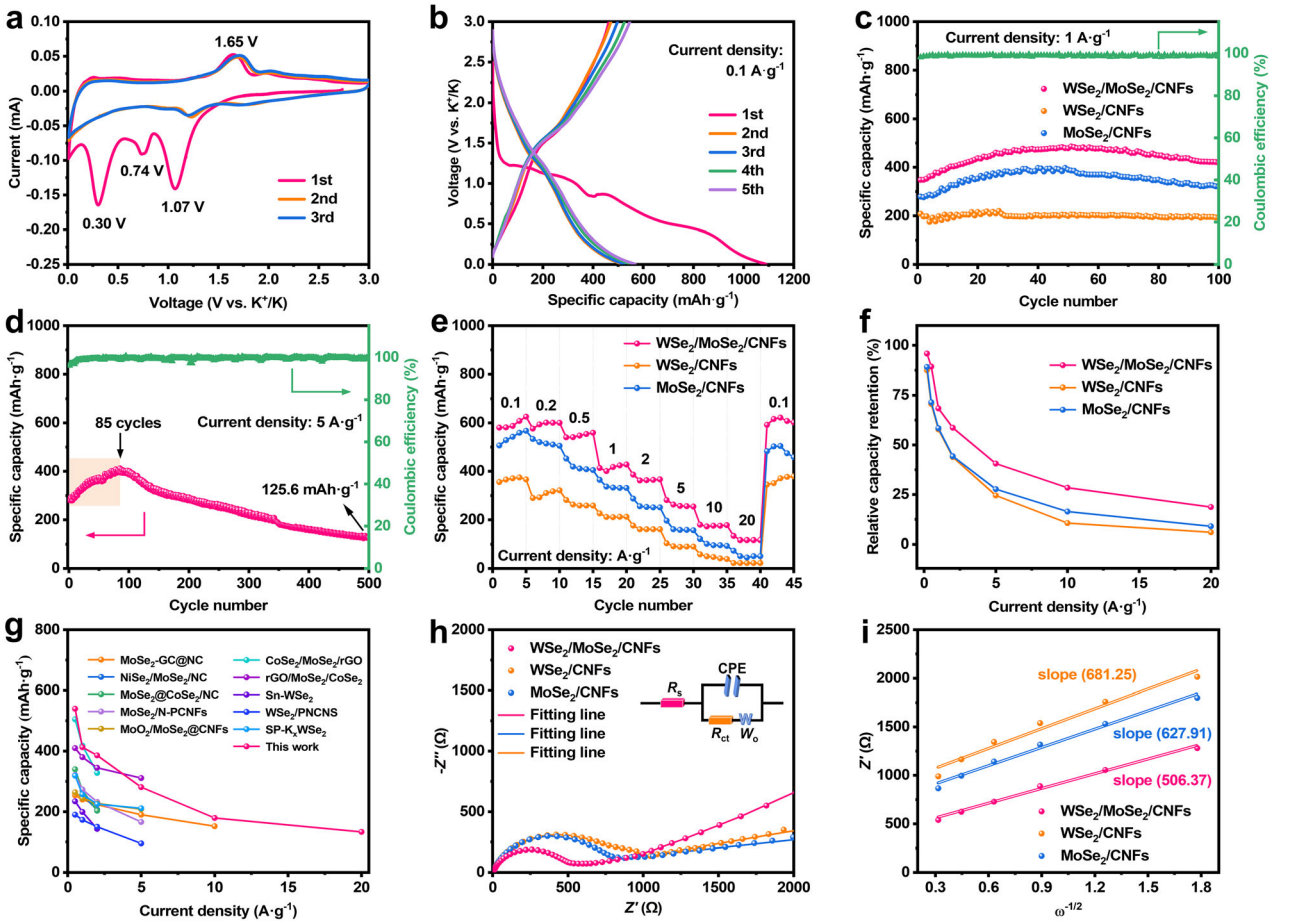

Fig. 3 Electrochemical performance for PIBs: **a** CV curves of $WSe_2/MoSe_2$/CNFs at 0.1 $mV{\cdot}s^{-1}$ in a voltage range of 0.005–3.0 V; **b** discharge/charge curves of $WSe_2/MoSe_2$/CNFs at 0.1 $A{\cdot}g^{-1}$; **c** cycling performance of $WSe_2/MoSe_2$/CNFs, WSe_2/CNFs, and $MoSe_2$/CNFs at 1 $A{\cdot}g^{-1}$ (after initial 3 cycles at 0.1 $A{\cdot}g^{-1}$); **d** long-term cycling performance of $WSe_2/MoSe_2$/CNFs at a current density of 5 $A{\cdot}g^{-1}$ (after the first three cycles at 0.1 $A{\cdot}g^{-1}$); **e** comparison of rate performance of $WSe_2/MoSe_2$/CNFs, WSe_2/CNFs, and $MoSe_2$/CNFs anodes; **f** comparison of rate capacity retention of three samples based on **e**; **g** comparison of rate performance with other reported similar anode materials; **h** Nyquist plots and equivalent circuit model of $WSe_2/MoSe_2$/CNFs, WSe_2/CNFs, and $MoSe_2$/CNFs; **i** the corresponding plots of the real part of impedance (Z') as a function of inverse square root of angular frequency ($\omega^{-1/2}$) in the Warburg region

were predicted to be 53.8%, 56.2%, and 59.3%, respectively. Combined with an inductively coupled plasma test (Table S2), the weight percentages of WSe_2 and $MoSe_2$ in the $WSe_2/MoSe_2$/CNF composite were 23.4% and 17.3%, respectively. From N_2 adsorption/desorption isotherms (Fig. S4a), the $WSe_2/MoSe_2$/CNFs showed a larger specific surface area of 33.4 $m^2{\cdot}g^{-1}$ than those of the WSe_2/CNFs (9.4 $m^2{\cdot}g^{-1}$) and $MoSe_2$/CNFs (15.8 $m^2{\cdot}g^{-1}$). The pore diameters of all composites were centered in the range of approximately 5–15 nm, indicating a mesopore structure (Fig. S4b). The high specific surface area and abundant mesopores provided more active sites and promoted ion diffusion, thereby improving the electrochemical performance of the $WSe_2/MoSe_2$/CNF electrode.

Cyclic voltammetry (CV) curves for $WSe_2/MoSe_2$/CNFs at a scan speed of 0.1 $mV{\cdot}s^{-1}$ and a potential range of 0.005–3.0 V are depicted in Fig. 3a (Fig. S5 for WSe_2/CNFs and $MoSe_2$/CNFs). During the initial cathodic scanning, the reduction peak at 1.07 V may have been due to the generation of K_xWSe_2/K_xMoSe_2 phases via K^+ intercalation, the peak at 0.74 V was ascribed to irreversible solid electrolyte interphase (SEI) layer formation resulting from the decomposition of the electrolyte, and the peak at 0.30 V was associated with K_xWSe_2/K_xMoSe_2 conversion to metallic W/Mo and K_2Se [38]. The peak at 1.65 V in the anodic scan was ascribed to oxidation that produced WSe_2 and $MoSe_2$ [27]. The CV curves for the succeeding cycles nearly overlap, demonstrating the better reversibility of $WSe_2/MoSe_2$/CNFs for potassium-ion batteries. The discharge and charge curves of the $WSe_2/MoSe_2$/CNFs with the potential range of 0.005–3.0 V and a current density of 0.1 $A{\cdot}g^{-1}$ are presented in Fig. 3b. The

initial discharge and charge capacities were 1088.6 and 463.4 mAh·g^{-1}, respectively, and the generation of the SEI was primarily responsible for the enormous capacity loss. The subsequent cycle processes exhibited overlaps in the voltage profiles, and the steady voltage platforms agreed with the CV test. The cyclic stabilities of the electrodes for the $WSe_2/MoSe_2$/CNFs, WSe_2/CNFs, $MoSe_2$/CNFs, and CNFs at 0.1 A·g^{-1} are shown in Fig. S6. In the 50th cycle, the $WSe_2/MoSe_2$/CNFs maintained a high discharge capacity of 483.8 mAh·g^{-1}. In comparison, after 50 cycles, the discharge capacities of the WSe_2/CNFs and $MoSe_2$/CNFs drop rapidly to 331.5 mAh·g^{-1} and 409.6 mAh·g^{-1}, respectively. The CNFs exhibited a capacity of 99.2 mAh·g^{-1} after 50 cycles. Therefore, it can be deduced that WSe_2 and $MoSe_2$ account for the majority of the capacity contribution in $WSe_2/MoSe_2$/CNFs. Figure 3c displays the cycle performance of the $WSe_2/MoSe_2$/CNFs, WSe_2/CNFs, and $MoSe_2$/CNF electrodes at 1 A·g^{-1}. The specific capacity of $WSe_2/MoSe_2$/CNFs stabilized at 426.1 mAh·g^{-1} over 100 cycles after pre-stabilization with three cycles at a low current density of 0.1 A·g^{-1}. This was considerably greater than that of WSe_2/CNFs (195.2 mAh·g^{-1}) and $MoSe_2$/CNFs (326.3 mAh·g^{-1}). In addition, the $WSe_2/MoSe_2$/CNF anode also delivered a relatively high Coulombic efficiency of nearly 99.0%. As shown in Fig. 3d, long-term cycling of the $WSe_2/MoSe_2$/CNFs was carried out at an elevated current density of 5 A·g^{-1}. A higher reversible capacity of 125.6 mAh·g^{-1} with 99.4% Coulombic efficiency was achieved up to 500 cycles. Notably, a gradual increase in the specific capacity was observed at the beginning of the galvanostatic charge/discharge tests (Fig. 3c, d). In view of this phenomenon, the electrochemical impedance spectroscopy (EIS) tests were conducted for different cycles at 5 A·g^{-1} (Fig. S7). The fresh cell showed a larger K^+ diffusion resistance of 539 Ω, which was rapidly reduced to 272 Ω after only 10 cycles. As the number of cycles increased, the K^+ diffusion resistance gradually reduced to 215, 147, and 107 Ω at the 20th, 40th, and 80th cycles, respectively, which was in line with the gradual capacity increase. These results can be attributed to the KFSI electrolyte, which electrochemically activates the electrode materials and extends the potassification duration [39]. HRTEM was used to characterize the $WSe_2/MoSe_2$/CNF electrode in the initial fully discharged/charged states at 5 A·g^{-1}. In the fully discharged state at 0.005 V (Fig. S8a), the lattice fringe was indexed to the (220) plane of K_2Se. In the charged state at 3.0 V, the lattice fringe was indexed to the (004) plane of WSe_2 or $MoSe_2$ (Fig. S8b). This result indicates the structural stability and reversibility of $WSe_2/MoSe_2$/CNFs during the initial charge and discharge processes. Subsequently, the evolution process of the $WSe_2/MoSe_2$/CNF electrode in the 5th, 25th, 50th, 100th, 200th, 300th, 400th and 500th cycles was characterized (Fig. S8c–j). With increase in cycling, the visualized crystalline regions of the material gradually decrease, while clear lattice fringes can still be observed, which corresponds to the cycle performance, as shown in Fig. 3d. The cyclic performance of $WSe_2/MoSe_2$/CNFs was further tested from the 500th to the 700th cycle at 5 A·g^{-1} (Fig. S9a). It should be noted that the degradation of the capacity with a longer cyclic test was possibly due to the deformation of the crystal structure (Fig. S9b, S9c).

Figure 3e shows a comparison of the rate capabilities of the three samples. The $WSe_2/MoSe_2$/CNF electrode exhibited specific capacities of 580.6, 576.5, 540.5, 413.7, 386.2, 281.3, 179.5 and 133.4 mAh·g^{-1} at 0.1, 0.2, 0.5, 1, 2, 5, 10 and 20 A·g^{-1}, respectively. As the current density turned to 0.1 A·g^{-1}, the reversible capacity quickly recovered to 592.1 mAh·g^{-1}, indicating that it can withstand the variations of various current densities. As shown in Fig. 3f, the $WSe_2/MoSe_2$/CNF electrode sustains excellent capacity retention at various current densities. Furthermore, a rate behavior comparison of the as-prepared materials is shown in Fig. 3g, and the observations suggest that $WSe_2/MoSe_2$/CNFs have obvious advantages over other anode materials [23, 25, 27, 30, 40–45]. The prominent potassium storage ability of $WSe_2/MoSe_2$/CNFs can be ascribed to the fact that $WSe_2/MoSe_2$, with a better-matched and stable heterojunction interface, enhances the useful area of the built-in electric field, which leads to a higher charge flux rate and faster potassium-ion diffusion kinetics, guaranteeing the realization of outstanding electrochemical properties. Figure 3h shows the EIS of the three-electrode materials. The results revealed that $WSe_2/MoSe_2$/CNFs with a smaller charge transfer resistance (R_{ct}) are indicative of a lower resistivity and faster electron/ion transfer rate [39]. In order to corroborate this, Fig. 3i illustrates the relation plot between the real part of impedance (Z') and the angular frequency ($\omega^{-1/2}$) in the low-frequency Warburg region. The linear slope value presents Warburg coefficient (σ), and it is related to the K^+ diffusion coefficient (D). The small σ indicates the large K^+ diffusion coefficient [46]. The relevant values were calculated based on the following formulas [47]:

$$Z' = R_{SEI} + R_{ct} + \sigma\omega^{-1/2} \quad (1)$$

$$D_{K^+} = R^2T^2/2A^2n^4F^4C^2\sigma^2 \quad (2)$$

where R_{SEI}, R, T, A, n, F, and C denote the resistance of the SEI, gas constant, absolute temperature, zone area at the electrode interface, electron concentration involved in the electrochemical process, Faraday's constant, and K^+ concentration in the electrode material, respectively. The slope value of $WSe_2/MoSe_2$/CNFs (506.37) was evidently less than those of WSe_2/CNFs (681.25) and $MoSe_2$/CNFs (627.91), representing a higher K^+ diffusion coefficient, which indicates enhanced K^+ transfer kinetics during the

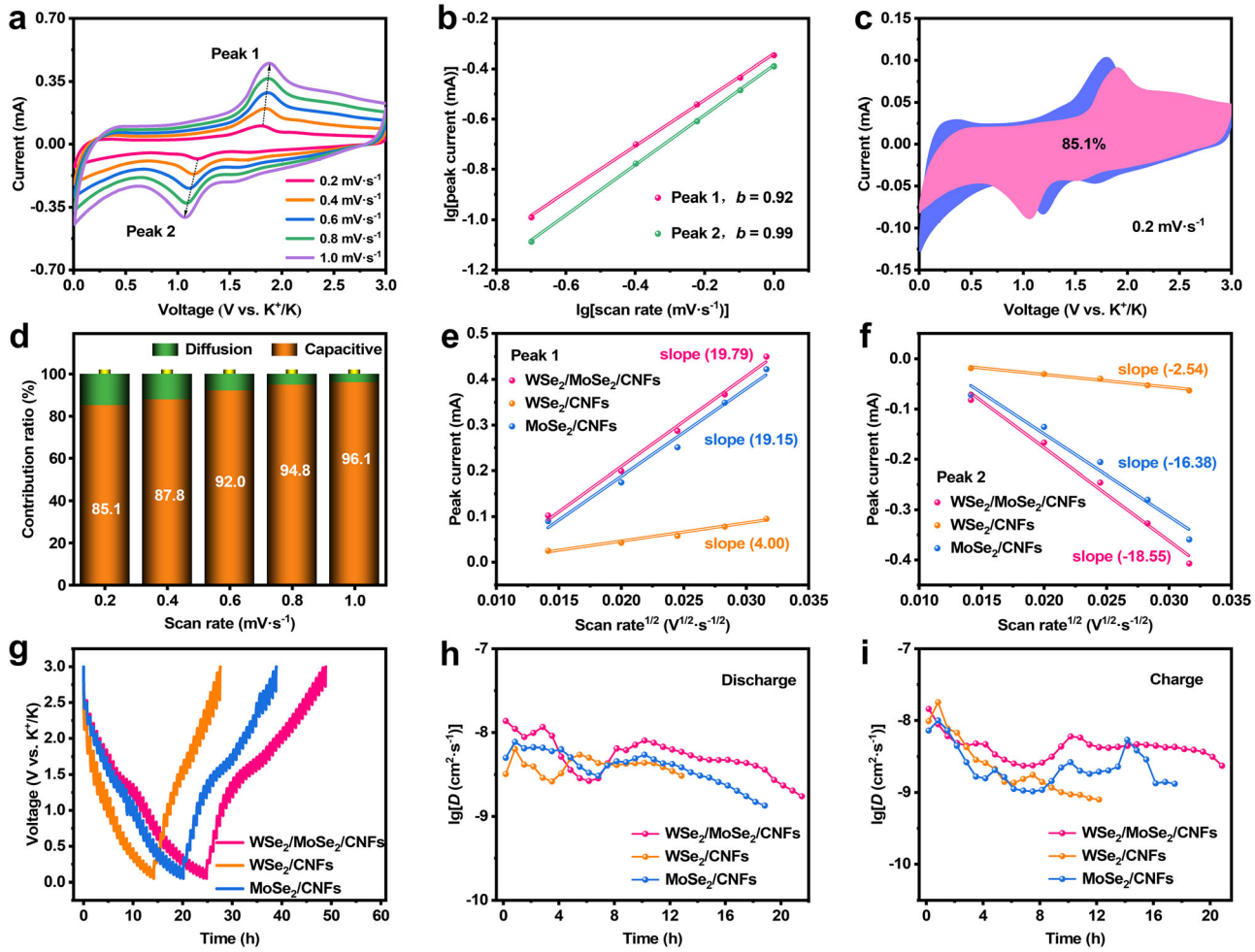

Fig. 4 Reaction kinetics analyses for PIBs: **a** CV curves of $WSe_2/MoSe_2$/CNFs in potential range of 0.005–3.0 V with different scan rates; **b** *b* value analysis using relationship between peak currents and scan rates for $WSe_2/MoSe_2$/CNFs; **c** capacitive contribution (pink region) of $WSe_2/MoSe_2$/CNFs for K^+ storage at 0.2 $mV{\cdot}s^{-1}$; **d** ratios of capacitive contribution at different scan rates for $WSe_2/MoSe_2$/CNFs; **e**, **f** plots of peak current versus square root of scan rate; **g–i** GITT curves and K^+ ionic diffusion coefficients as a function of time for $WSe_2/MoSe_2$/CNFs, WSe_2/CNFs, and $MoSe_2$/CNFs

electrochemical reaction process of the $WSe_2/MoSe_2$/CNF electrode. Figure S10 shows the EIS curves of the $WSe_2/MoSe_2$/CNFs, WSe_2/CNFs, and $MoSe_2$/CNF electrodes after 500 cycles at 5 $A{\cdot}g^{-1}$. $WSe_2/MoSe_2$/CNFs still exhibited the lowest impedance compared to WSe_2/CNFs and $MoSe_2$/CNFs, which is mainly attributed to the coupling of the different components to form a heterostructure that can accelerate charge transfer and enhance structural integrity. This results in excellent cycling performance.

To investigate the kinetic behavior of K^+ storage in the $WSe_2/MoSe_2$/CNF anode, CV tests were performed at various scan speeds (Fig. 4a). The connection between the scan rate (v) and peak current (i) can be presented as follows [48]:

$$i = av^b \tag{3}$$

The b value was determined using the slope of a lg$v$ versus lg$i$ plot. When b value was close to 1, capacitive behavior was predominant in the electrochemical process. Moreover, the electrochemical reaction was mainly governed by the ion diffusion behavior when b value was near 0.5. As shown in Fig. 4b, the acquired b values of peak 1 and peak 2 are 0.92 and 0.99, respectively, which reveals that the capacitive behavior dominates the discharge/charge processes of $WSe_2/MoSe_2$/CNFs. Equation (4) was used to quantify the capacitive contribution at different scan speeds [49].

$$i = k_1 v + k_2 v^{1/2} \tag{4}$$

The contributions of the pseudocapacitance and diffusion behavior to the reactions are represented by $k_1 v$ and $k_2 v^{1/2}$, respectively. At the low scanning rate of 0.2 $mV{\cdot}s^{-1}$, as demonstrated in Fig. 4c, the contribution of pseudocapacitive behavior was 85.1%. The percentage contribution of capacitance increased as the scan rate

increased (Fig. 4d). The high pseudocapacitive behavior is attributed to the constructed heterogeneous structure, which can enhance the K^+ transport kinetics. WSe_2/$MoSe_2$ nanosheets with large specific surface areas are also beneficial for the fast storage of K^+. Therefore, the remarkable cycling performance and rate behavior of the WSe_2/$MoSe_2$/CNF anode can be explained by its high pseudocapacitive contribution. The Randles–Sevcik equation was used to determine the K^+ diffusion coefficient using a set of CV curves (Figs. 4a, S11) [30]:

$$I_p = 2.69 \times 10^5 D^{1/2} n^{3/2} v^{1/2} A C_0 \quad (5)$$

A positive correlation was observed between the K^+ diffusion coefficient and slopes of the curves ($I_p/v^{1/2}$). Clearly, WSe_2/$MoSe_2$/CNFs displayed the highest slopes among the three samples (Fig. 4e, f), indicating a faster diffusion rate of K^+. The galvanostatic intermittent titration technique (GITT) was used to further analyze the potassium storage kinetics for as-prepared electrodes (Fig. 4g). The K^+ diffusion coefficients of the WSe_2/$MoSe_2$/CNFs, WSe_2/CNFs, and $MoSe_2$/CNFs were determined using the following equation [26]:

$$D_{K^+} = \frac{4L^2}{\pi\tau}\left(\frac{\Delta E_s}{\Delta E_t}\right)^2 \quad (6)$$

where τ is the current pulse time, ΔE_s is the deviation of each equilibrium voltage, ΔE_t is the deviation voltage during the current pulse, and L is the average thickness of the electrode. The single-step GITT measurement yielded the parameters for computing the K^+ diffusion coefficient, as illustrated in Fig. S12. Figure 4h, i demonstrates the relevant K^+ diffusion coefficients for the discharge and charge cycles. The K^+ diffusion coefficients of WSe_2/$MoSe_2$/CNFs were significantly larger than those of WSe_2/CNFs and $MoSe_2$/CNFs during the entire charge/discharge process, suggesting faster electrochemical reaction kinetics, which is advantageous for supporting the outstanding rate property and cycling durability of the WSe_2/$MoSe_2$/CNF anode.

In situ XRD measurements were performed to investigate the potassium storage mechanism of WSe_2/$MoSe_2$/CNFs (Fig. 5a). The initial discharge/charge process was performed in an in situ cell with a potential range of 0.005 to 3.0 V. The increase in intensity is indicated by a color change from blue to red in the diffraction peaks. Throughout the cycling process, the diffraction peaks of Be (41.3°) and BeO (38.7° and 44.0°) did not change [50]. Strong characteristic peaks at 13.8°, 28.6° and 41.9° were observed for the WSe_2/$MoSe_2$/CNFs in their pristine state, which matched the (002), (004), and (006) planes of WSe_2/$MoSe_2$, respectively. With further discharging, the strength of these feature peaks progressively weakened, and three broad peaks related to the K_2Se planes appeared at 10.4°, 20.7° and 33.5°, indicating that the conversion reaction involved an intermediate product of K_2Se [23]. However, for W and Mo, no distinctive reflections were observed at this stage, which may be due to their amorphous nature or small crystallite sizes. The peak intensity of K_2Se gradually decreased and eventually disappeared throughout the charging process, indicating the occurrence of a reverse conversion reaction between K_2Se and W/Mo selenides. In the fully charged state, the peak of WSe_2/$MoSe_2$ reappeared at approximately 13.8°, whereas the other peaks did not resurface, which might be partially explained by the poor crystallinity or small particle size of WSe_2/$MoSe_2$ after undergoing potassium removal [51]. A similar phenomenon is shown in Fig. 5b. As seen from Fig. S13, the (002) characteristic peak of WSe_2/$MoSe_2$ moved slightly to a lower angle during potassiation, suggesting that K^+ intercalates into WSe_2/$MoSe_2$ to form K_xWSe_2/K_xMoSe_2. Subsequently, to further study the changes in the chemical components, ex situ XPS of the WSe_2/$MoSe_2$/CNF anode was performed at various reaction stages. As observed in Fig. 5c, the peaks at approximately 228.3 and 233.1 eV were identified as being for Mo^{4+} after being discharged to 0.005 V. The peaks at 226.5 and 230.6 eV belonged to elemental Mo^0, representing the reduction of $MoSe_2$ to Mo metal [26]. Only the peaks of Mo^{4+} were visible when the cell was recharged to 3.0 V, demonstrating the reversibility of $MoSe_2$ during potassification and depotassification. For W 4f spectra (Fig. 5d), when discharging to 0.005 V, it displayed the presence of metallic W^0 at 35.4 eV and 37.6 eV, accompanied by the potassiation process [31]. However, W^0 was not fully oxidized after being fully charged, indicating the partial reversibility of the conversion process of WSe_2. This phenomenon can also explain why WSe_2/CNFs display poor electrochemical performance compared to $MoSe_2$/CNFs. Importantly, according to the above discussion, the potassium storage mechanism of the WSe_2/$MoSe_2$/CNF anode is summarized as follows:

Discharged process:

$$WSe_2 + xK^+ + xe^- \rightarrow K_xWSe_2 \quad (7)$$

$$MoSe_2 + xK^+ + xe^- \rightarrow K_xMoSe_2 \quad (8)$$

$$K_xWSe_2 + (4-x)K^+ + (4-x)e^- \rightarrow W + 2K_2Se \quad (9)$$

$$K_xMoSe_2 + (4-x)K^+ + (4-x)e^- \rightarrow Mo + 2K_2Se \quad (10)$$

Charged process:

$$W + 2K_2Se \rightarrow WSe_2 + 4K^+ + 4e^- \quad (11)$$

$$Mo + 2K_2Se \rightarrow MoSe_2 + 4K^+ + 4e^- \quad (12)$$

The influence mechanism of the WSe_2/$MoSe_2$ heterojunction interface on K^+ storage was further

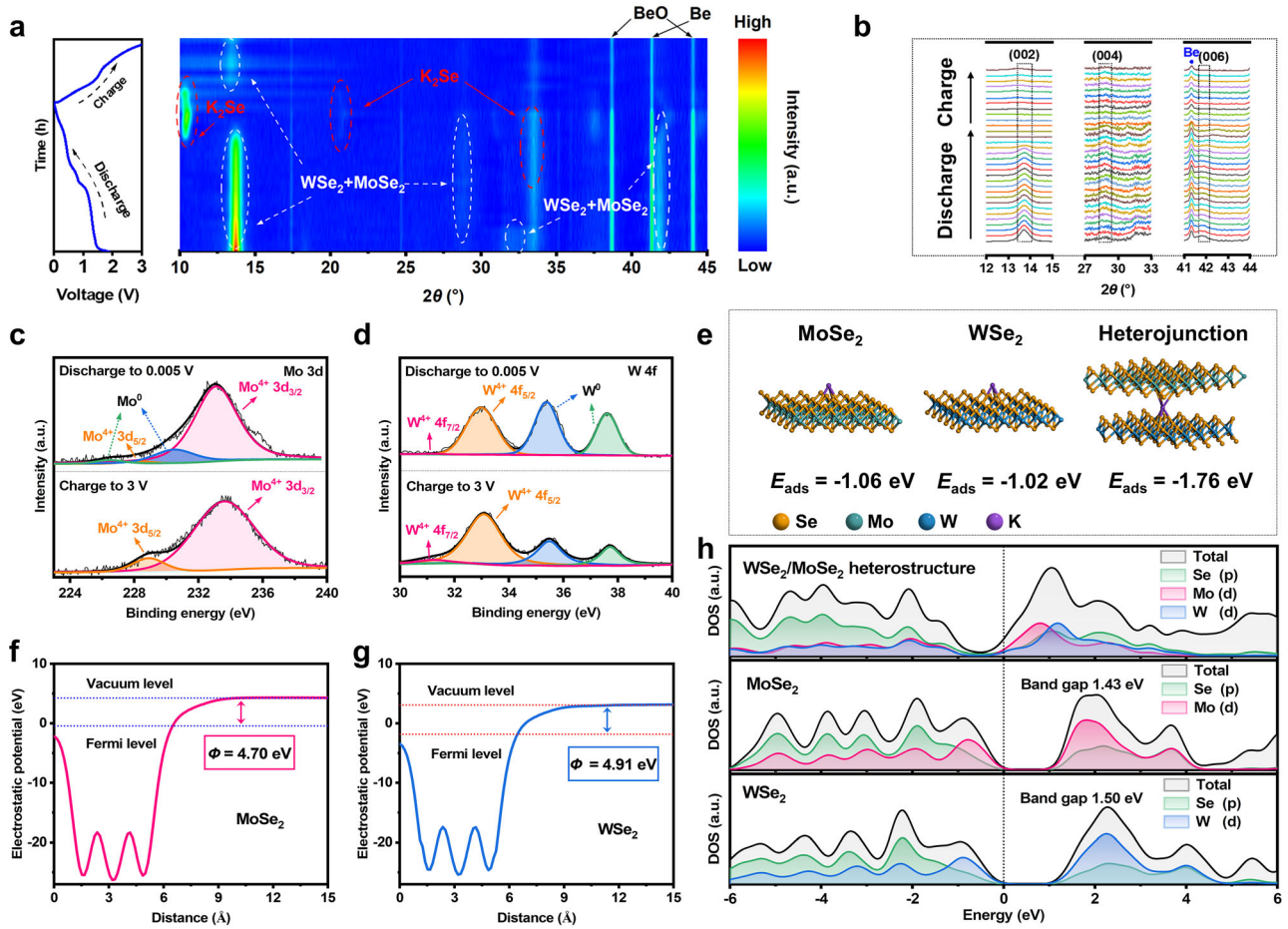

Fig. 5 Reaction mechanism exploration of $WSe_2/MoSe_2$/CNFs anode for PIBs: **a** contour plots of in situ XRD analysis at a cutoff voltage of 0.005–3.0 V during initial cycle; **b** fine XRD diffraction spectra under different discharge and charge states; ex situ high-resolution **c** Mo 3d and **d** W 4f XPS spectra of $WSe_2/MoSe_2$/CNFs at fully discharged (0.005 V) and charged (3.0 V) states; **e** side views of potassium adsorption energies in $MoSe_2$, WSe_2, and $WSe_2/MoSe_2$ heterojunction interface, respectively; electrostatic potentials of **f** $MoSe_2$ and **g** WSe_2; **h** DOS of $WSe_2/MoSe_2$ heterostructure, $MoSe_2$, and WSe_2

studied using DFT calculations. Figures 5e, S14 show the side and top views of the adsorption models, as well as the adsorption energy (E_{ads}) values of the WSe_2, $MoSe_2$, and $WSe_2/MoSe_2$ heterostructures for potassium. The adsorption energy of potassium on the $WSe_2/MoSe_2$ heterointerface (− 1.76 eV) was remarkably lower compared with those of WSe_2 (− 1.02 eV) and $MoSe_2$ (− 1.06 eV), suggesting that the potassium is more handily adsorbed on the $WSe_2/MoSe_2$ heterointerface. Figure 5f, g illustrates that $MoSe_2$ displayed a lower work function (4.70 eV) than WSe_2 (4.91 eV), demonstrating that the electrons in $MoSe_2$ move to WSe_2 to reach uniform Fermi levels once the heterointerface is built. As demonstrated in Fig. S15, an additional electromotive force that promotes electron migration was provided by the built-in electric field pointing from WSe_2 to $MoSe_2$; the $MoSe_2$ side was surrounded by a positively charged space, whereas the WSe_2 side was covered by a negatively charged space. Figure S16 shows the band structures of the $MoSe_2$, WSe_2, and $WSe_2/MoSe_2$ heterostructures. Clearly, $MoSe_2$ and WSe_2 exhibited semiconducting characteristics. In contrast, the constructed $WSe_2/MoSe_2$ heterojunction shows that the electrons cross the Fermi level, and the conductivity is greatly improved. Compared to the band gap values of $MoSe_2$ and WSe_2, the $WSe_2/MoSe_2$ heterostructure exhibited distinct metallic properties (Fig. 5h) [52]. Moreover, the Mo d and W d orbitals of the $WSe_2/MoSe_2$ heterojunction showed a similar distribution trend to $MoSe_2$ and WSe_2, which play a major energy-level contributing role at positions near the Fermi level. The new electronic states generated by Mo and W in the conduction band of the $WSe_2/MoSe_2$ heterojunction increased the carrier concentration, accelerated electron transfer, and improved the conductivity of the $WSe_2/MoSe_2$ heterojunction. These advantages effectively improved the energy storage performance of PIBs.

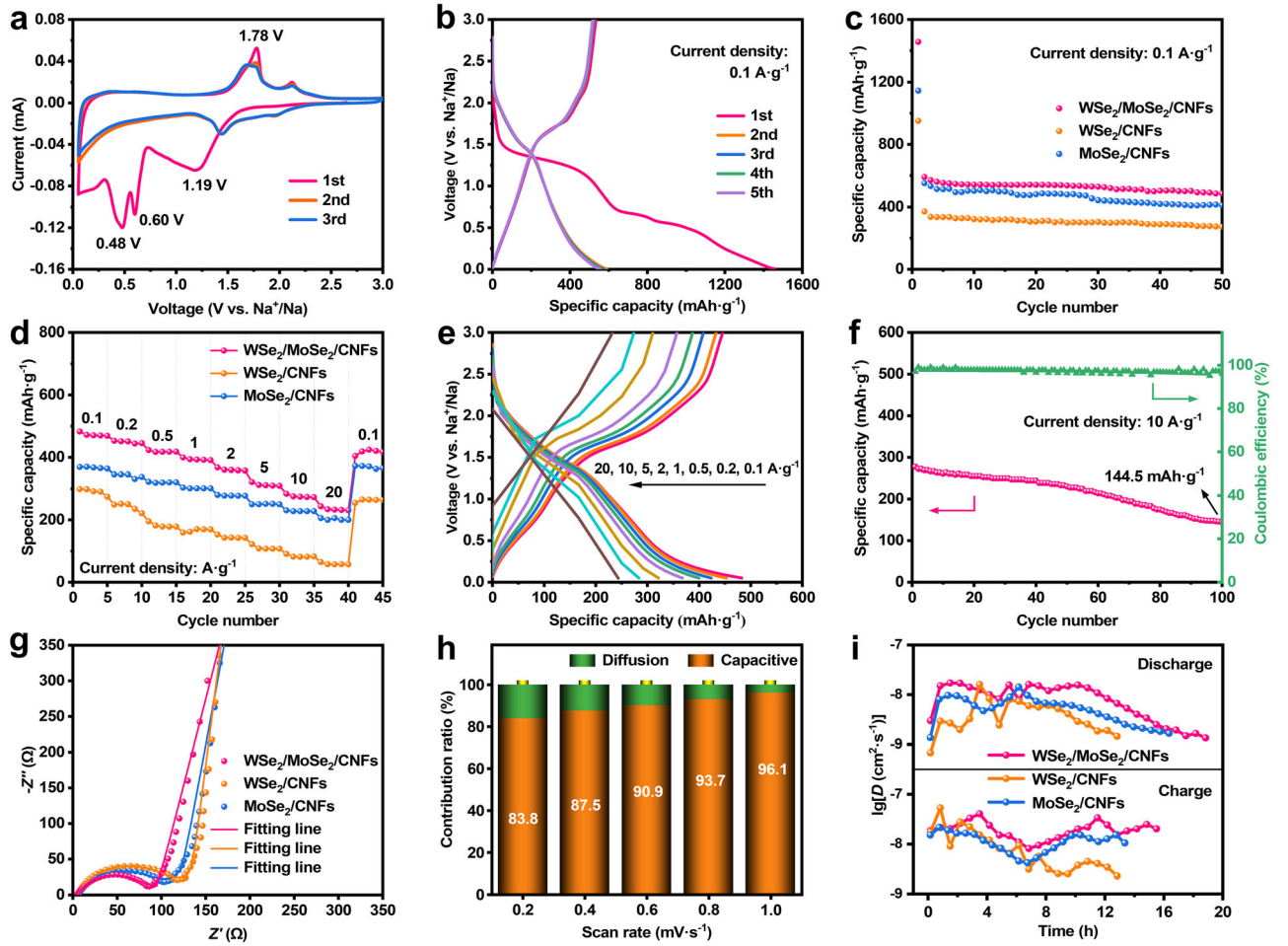

Fig. 6 Electrochemical properties and kinetic analysis for SIBs: **a** CV curves of $WSe_2/MoSe_2$/CNFs at 0.1 mV·s^{-1}; **b** charge/discharge curves at 0.1 A·g^{-1} for $WSe_2/MoSe_2$/CNFs; **c** cycling performance of $WSe_2/MoSe_2$/CNFs, WSe_2/CNFs, and $MoSe_2$/CNFs at 0.1 A·g^{-1}; **d** rate performance at various current densities from 0.1 to 20 A·g^{-1}; **e** charge/discharge curves of $WSe_2/MoSe_2$/CNFs anode at different current densities; **f** long-term cycling performance of $WSe_2/MoSe_2$/CNFs at 10 A·g^{-1} (after initial three cycles at 0.1 A·g^{-1}); **g** EIS curves of $WSe_2/MoSe_2$/CNFs, WSe_2/CNFs, and $MoSe_2$/CNFs; **h** ratios of capacitive contribution at different scan rates for $WSe_2/MoSe_2$/CNFs; **i** Na^+ ionic diffusion coefficients as a function of time for $WSe_2/MoSe_2$/CNFs, WSe_2/CNFs, and $MoSe_2$/CNFs

SIBs were assembled to investigate the sodium storage properties of the as-prepared composites. As shown in Fig. 6a, a CV test of $WSe_2/MoSe_2$/CNFs was performed at 0.1 mV·s^{-1} (Fig. S17 for WSe_2/CNFs and $MoSe_2$/CNFs). In the initial cathodic reaction, the reduction peak located at 1.19 V resulted from Na^+ intercalation in $WSe_2/MoSe_2$ to generate Na_xWSe_2/Na_xMoSe_2, the SEI film formation was confirmed in the peak at 0.60 V, and the conversion of Na_xWSe_2/Na_xMoSe_2 into metallic W/Mo and Na_2Se was offered by another peak at 0.48 V [37]. The subsequent anodic curve exhibits one oxidation peak at 1.78 V, which was linked to the transformation of W/Mo into $WSe_2/MoSe_2$ [53]. Clearly, minor changes in the CV curves can be seen in the following two cycles, demonstrating the outstanding electrochemical reversibility of the $WSe_2/MoSe_2$/CNF anode. Figure 6b shows the discharge and charge curves of the $WSe_2/MoSe_2$/CNF anode in the first five cycles at 0.1 A·g^{-1}. The comparatively low Coulombic efficiency during the first cycle can be attributed to the irreversible capacity loss caused by the formation of the SEI film. In addition, the 3rd, 4th, and 5th charge/discharge cycles almost exactly coincided with the 2nd cycle, revealing the outstanding reversibility of $WSe_2/MoSe_2$/CNFs for Na^+ storage. Figure 6c compares the cycling stabilities of the three-electrode materials at 0.1 A·g^{-1}. After 50 cycles, the $WSe_2/MoSe_2$/CNF composite exhibited a discharge capacity of 484.9 mAh·g^{-1}, outperforming the WSe_2/CNFs (273.2 mAh·g^{-1}) and $MoSe_2$/CNFs (411.4 mAh·g^{-1}). Furthermore, the $WSe_2/MoSe_2$/CNF electrode exhibited a superior rate performance (Fig. 6d). At current densities of 0.1, 0.2, 0.5, 1, 2, 5, 10 and 20 A·g^{-1}, the discharge specific capacities were 482.5, 452.9, 423.3, 399.6, 367.6, 322.0, 283.6 and 243.5 mAh·g^{-1}, respectively. The discharge capacity increased to 417.1 mAh·g^{-1}

when the current density was brought back to 0.1 $A{\cdot}g^{-1}$. The discharge/charge profiles of $WSe_2/MoSe_2$/CNFs with current densities from 0.1 to 20 $A{\cdot}g^{-1}$ are shown in Fig. 6e. The shapes of the discharge and charge profiles are almost identical at different current densities, proving the reversibility of the $WSe_2/MoSe_2$/CNFs. A comparison of the rate performance of $WSe_2/MoSe_2$/CNFs with those of other relevant anode materials is shown in Fig. S18. The prepared $WSe_2/MoSe_2$/CNFs exhibited excellent electrochemical performance as anodes for SIBs. Additionally, a prolonged cycling test under 10 $A{\cdot}g^{-1}$ was performed (Fig. 6f). It is noteworthy that the $WSe_2/MoSe_2$/CNF anode could deliver a superior reversible capacity of 144.5 $mAh{\cdot}g^{-1}$ and a high Coulombic efficiency of 97.3% after 100 cycles. Although the $WSe_2/MoSe_2$/CNF electrode exhibited an increase in the capacity for potassium storage in the first few tens of cycles, this phenomenon was not observed in SIBs. This difference can be attributed to the sluggish diffusion of K^+, which has a relatively large ionic radius, and slow penetration of the KFSI electrolyte into the electrode via electrochemical activation [30, 39].

The electrochemical resistances of the as-prepared samples were examined by EIS (Fig. 6g). The results reveal that the $WSe_2/MoSe_2$/CNFs showed lower charge transfer resistance compared to the WSe_2/CNFs and $MoSe_2$/CNFs, indicating superior electrical conductivity. Meanwhile, the lower slope value of the $WSe_2/MoSe_2$/CNFs means more rapid Na^+ transfer and increased reaction kinetics (Fig. S19). The CV curves at various scan speeds were used to evaluate the electrochemical kinetic behavior of the $WSe_2/MoSe_2$/CNFs (Fig. S20a). The two major peaks of the $WSe_2/MoSe_2$/CNF anode were observed in the electrochemical process at b values of 0.93 and 0.90 (Fig. S20b). All b values were close to 1, indicating that the capacitance process was dominant and the $WSe_2/MoSe_2$/CNF electrode possesses ultrafast Na^+ diffusion kinetics. Figure S21 shows the detailed capacitive contribution (83.8%) to the overall sodium storage at 0.2 $mV{\cdot}s^{-1}$, based on quantity measurements. The capacitive contribution percentages of the $WSe_2/MoSe_2$/CNF electrode at different scan speeds are shown in Fig. 6h. These findings demonstrate that potassium and sodium storage have comparable electrochemical behaviors. The surface pseudocapacitive contributions were, respectively, 83.8%, 87.5%, 90.9%, 93.7% and 96.1% of the entire capacity when scanning speed increases from 0.2 to 1.0 $mV{\cdot}s^{-1}$. The surface pseudocapacitive mechanism was dominant in the sodium storage process, particularly at high scan rates. In addition, CV curves were obtained at various scanning speeds to further explore the sodium storage kinetics (Figs. S20a, S22). The highest slope values of the $WSe_2/MoSe_2$/CNF anode among all the samples indirectly indicated the rapid diffusion kinetics of sodium ions, which is conducive to the greater rate performance and cycle durability of the $WSe_2/MoSe_2$/CNF anode. GITT tests of the three anodes were carried out by utilizing a range of pulse current at 0.1 $A{\cdot}g^{-1}$ for 10 min and a relaxation time of 30 min during the initial cycle stages (Fig. S23). The $WSe_2/MoSe_2$/CNFs exhibited smaller polarization and higher diffusion coefficients in both the sodiation and desodiation processes (Fig. 6i), which further verifies the accelerated Na^+ transport behavior. Based on the investigations of the electrochemical reaction kinetics presented above, the steady cycle lifespan and excellent rate stability of the $WSe_2/MoSe_2$/CNFs can be explained by the dominant pseudocapacitive behavior and accelerated sodium-ion migration kinetics.

Based on the above discussion, $WSe_2/MoSe_2$/CNFs as anode materials in PIBs and SIBs exhibit remarkable advantages, which are mainly due to the following reasons. (1) The heterogeneous structure constructed by WSe_2 and $MoSe_2$ with better matching elevates the effective contact area of the heterointerface, which supplies numerous active sites and enlarges the utilization range of the built-in electric field to hasten the transport of electrons/ions and further accelerates the cycling kinetics. (2) The ultra-high pseudocapacitance contribution originating from the heterostructure and morphological features of the $WSe_2/MoSe_2$ nanosheets is conducive to enhancing high-rate energy storage. (3) The incorporation of 1D carbon nanofibers as a sturdy skeleton substrate to support the $WSe_2/MoSe_2$ nanosheets not only increases the conductivity of the composite but also mitigates the large volume change of the anode upon electrochemical cycling, achieving a relatively stable cycling performance and long cycle life.

4 Conclusion

In summary, an advanced PIB/SIB anode material based on a $WSe_2/MoSe_2$/CNFs heterostructure is reported, fabricated through a facile synthesis process that incorporates the electrospinning of a 1D fiber template and the surface in situ growth of $WSe_2/MoSe_2$ nanosheets. This hierarchical structure restrains the volume expansion of the active material during cycling. The $WSe_2/MoSe_2$ heterojunction interface, with better matching and stability, displayed a strong potassium adsorption energy, which facilitated the provision of effective active sites and rapid ion storage at the interface. The enlarged effective utilization range of the built-in electric field at the heterointerface provided a powerful driving force for accelerating the transfer of electrons and ions, thus enabling an exceptional cycling capability. In addition, the contribution of ultra-high pseudocapacitance was beneficial for enhancing high-rate energy storage. As expected, the

$WSe_2/MoSe_2$/CNF composite exhibits excellent rate performance (133.4 $mAh{\cdot}g^{-1}$ at 20 $A{\cdot}g^{-1}$) and cycling stability (125.6 $mAh{\cdot}g^{-1}$ over 500 cycles at 5 $A{\cdot}g^{-1}$) when used as the PIB anode. High-rate performance was also realized in sodium-ion storage (243.5 $mAh{\cdot}g^{-1}$ at 20 $A{\cdot}g^{-1}$). This study incorporates the advantages of heterogeneous interface engineering and structural regulation in the construction of PIB/SIB anodes, offering a potential strategy for high-performance energy storage materials.

Acknowledgements This work was financially supported by the National Natural Science Foundation of China (No. 22201098), the Natural Science Foundation of Shandong Province (Nos. ZR202 1QB005 and ZR2021MB008), and Jinan City "New University 20" Project (No. 202228113).

Declarations

Conflict of interests The authors declare that they have no conflict of interest.

References

[1] Lin XP, Xue FF, Zhang ZG, Li QH. Sb nanoparticles encapsulated in N-doped carbon nanotubes as freestanding anodes for high-performance lithium and potassium ion batteries. Rare Met. 2023;42(2):449. https://doi.org/10.1007/s12598-022-02143-6.

[2] Zheng C, Chen CR, Lin C, Wei MD. CMK-5-encapsulated $MoSe_2$ composite for rechargeable lithium-ion batteries with improve electrochemical performance. J Mater Chem A. 2017;5(37):19632. https://doi.org/10.1039/C7TA06286A.

[3] Chen YX, Shi XD, Lu BG, Zhou J. Concave engineering of hollow carbon spheres toward advanced anode material for sodium/potassium-ion batteries. Adv Energy Mater. 2022;12(46):2202851. https://doi.org/10.1002/aenm.202202851.

[4] Yuan F, Shao YC, Wang B, Wu YS, Zhang D, Li ZJ, Wu YM. Recent progress in application of cobalt-based compounds as anode materials for high-performance potassium-ion batteries. Rare Met. 2022;41(10):3301. https://doi.org/10.1007/s12598-022-02052-8.

[5] Zhou M, Wang Q, Yuan Y, Luo SH, Zhang YH, Liu X. Biocarbon with different microstructures derived from corn husks and their potassium storage properties. Rare Met. 2021;40(11):3166. https://doi.org/10.1007/s12598-021-01775-4.

[6] Qi SH, Deng JW, Zhang WC, Feng YZ, Ma JM. Recent advances in alloy-based anode materials for potassium ion batteries. Rare Met. 2020;39(9):970. https://doi.org/10.1007/s12598-020-01454-w.

[7] Gao X, Wang T, Sun K, Fu YJ, Wu Y, Liu DQ, He DY. Construction of MoS_2-ZnS@C heterostructures by multiple organic framework combination for fast and stable sodium/potassium storage. ACS Appl Energy Mater. 2023;6(5):3081. https://doi.org/10.1021/acsaem.3c00012.

[8] Zhang SP, Ling FX, Wang LF, Xu R, Ma MZ, Cheng XL, Bai RL, Shao Y, Huang HJ, Li DJ, Jiang Y, Rui XH, Bai JT, Yao Y, Yu Y. An open-ended Ni_3S_2-Co_9S_8 heterostructures nanocage anode with enhanced reaction kinetics for superior potassium-ion batteries. Adv Mater. 2022;34(18):2201420. https://doi.org/10.1002/adma.202201420.

[9] Wang SY, Zhao R, Yao SY, Wang XX, Wang JR, Gao XY, Hou ZH, Liu X, Fu ZZ, Wang DW, Xie JZ, Yang ZY, Yan YM. Spatially expanded built-in electric field via engineering graded junction enables fast charge transfer in bulk MnO@Mn_3O_4 for Na^+ supercapacitors. Nano Energy. 2023;115:108725. https://doi.org/10.1016/j.nanoen.2023.108725.

[10] Zhou ZP, Zeng H, Li L, Tang RD, Xiong S, Gong DX, Huang Y, Deng YC. Internal electric fields drive dual S-scheme heterojunctions: insights into the role of the triple interlaced lattice. J Colloid Interf Sci. 2023;650:1138. https://doi.org/10.1016/j.jcis.2023.07.086.

[11] Dong Z, Wu X, Chen M, Chen HX, Huang KJ, Wang LL, Xu J. Self-supporting 1T-MoS_2@WS_2@CC composite materials for potential high-capacity sodium storage system. J Colloid Interf Sci. 2023;630:426. https://doi.org/10.1016/j.jcis.2022.10.072.

[12] Rao Y, Wang J, Liang PH, Zheng HJ, Wu M, Chen JT, Shi F, Yan K, Liu JS, Bian K, Zhang CX, Zhu KJ. Heterostructured WS_2/MoS_2@carbon hollow microspheres anchored on graphene for high-performance Li/Na storage. Chem Eng J. 2022;443:136080. https://doi.org/10.1016/j.cej.2022.136080.

[13] Li Q, Yu FY, Cui YR, Wang J, Zhao Y, Peng JH. SnS-SnO_2 heterostructures anchored on GO as a high-performance anode for sodium ion battery. Chem Eur J. 2023;29(23):202300009. https://doi.org/10.1002/chem.202300009.

[14] Fan W, Yuan H, Huang JG. A bio-inspired nanofibrous Co_3O_4/TiO_2/carbon composite as high-performance anodic material for lithium-ion batteries. J Alloy Compd. 2020;819:153375. https://doi.org/10.1016/j.jallcom.2019.153375.

[15] Je JH, Lim HJ, Jung HW, Kim SO. Ultrafast and ultrastable heteroarchitectured porous nanocube anode composed of CuS/FeS_2 embedded in nitrogen-doped carbon for use in sodium-ion batteries. Small. 2021;18(6):2105310. https://doi.org/10.1002/smll.202105310.

[16] Li LX, Zhang SQ, Wang WW, Lei HY, Liu XJ, Wang H. Heterojunction and carbon coating dual strategy mechanism: WSe_2/NiSe@C nanosheets for efficient sodium storage. Electroanal Chem. 2023;939:117467. https://doi.org/10.1016/j.jelechem.2023.117467.

[17] Zheng C, Wu JX, Li YF, Liu XJ, Zeng LX, Wei MD. High-performance lithium-ion based dual-ion batteries enabled by few-layer $MoSe_2$/Nitrogen-doped carbon. ACS Sustainable Chem Eng. 2020;8(14):5514. https://doi.org/10.1021/acssuschemeng.9b06815.

[18] Wang JB, Chen L, Zeng LX, Wei QH, Wei MD. In situ synthesis of WSe_2/CMK-5 nanocomposite for rechargeable lithium-ion batteries with a long-term cycling stability. ACS Sustainable Chem Eng. 2018;6(4):4688. https://doi.org/10.1021/acssuschemeng.7b03694.

[19] Chen DL, Zhao ZY, Chen GL, Li TT, Chen J, Ye ZZ, Lu JG. Metal selenides for energy storage and conversion: a comprehensive review. Coordin Chem Rev. 2023;479:214984. https://doi.org/10.1016/j.ccr.2022.214984.

[20] Cong BW, Li XR, Suo YH, Chen G. Metal-organic framework derived bimetallic selenide embedded in nitrogen-doped carbon hierarchical nanosphere for highly reversible sodium-ion storage. J Colloid Interf Sci. 2023;635:370. https://doi.org/10.1016/j.jcis.2022.12.153.

[21] Wang YY, Kang WP, Pu XJ, Liang YC, Xu B, Lu XQ, Sun DF, Cao YL. Template-directed synthesis of $Co_2P/MoSe_2$ in a N-doped carbon hollow structure for efficient and stable sodium/potassium ion storage. Nano Energy. 2022;93:106897. https://doi.org/10.1016/j.nanoen.2021.106897.

[22] Tian CX, Cui SY, Meng N, An Sam OJ, Wang DH, Jiang M, Zang Y, Xin Q, Yan WS, Lu L. Three-dimensional flower spheres $MoSe_2$/NiSe heterostructure with fast kinetic and stable structure for durable sodium-ion storage. Appl Surf Sci. 2023;616:156511. https://doi.org/10.1016/j.apsusc.2023.156511.

[23] Zhao ZC, Xu T, Yu XB. Unlock the potassium storage behavior of single-phased tungsten selenide nanorods via large cation insertion. Adv Mater. 2022;35(5):2208096. https://doi.org/10.1002/adma.202208096.

[24] Kang BY, Chen XC, Zeng LX, Luo FQ, Li XY, Xu LH, Yang MQ, Chen QH, Wei MD, Qian QR. In situ fabrication of ultrathin few-layered WSe_2 anchored on N, P dual-doped carbon by bioreactor for half/full sodium/potassium-ion batteries with ultralong cycling lifespan. J Colloid Interf Sci. 2020;574:217. https://doi.org/10.1016/j.jcis.2020.04.055.

[25] Xu YN, Liu XF, Su H, Jiang S, Zhang JM, Li D. Hierarchical bimetallic selenides $CoSe_2$-$MoSe_2$/rGO for sodium/potassium-ion batteries anode: insights into the intercalation and conversion mechanism. Energy Environ Mater. 2021;5(2):627. https://doi.org/10.1002/eem2.12206.

[26] Feng J, Luo SH, Li PW, Lin YC, Zhang L, Wang Q, Zhang YH. Unveiling the efficient sodium storage and mechanism of MOFs-induced CoSe@N-doped carbon polyhedrons decorated with 2H-$MoSe_2$ nanosheets. Appl Surf Sci. 2023;619:156775. https://doi.org/10.1016/j.apsusc.2023.156775.

[27] Yu L, He XY, Peng B, Wang WT, Wan GL, Ma XY, Zeng SY, Zhang GQ. Constructing ion diffusion highway in strongly coupled WSe_2-carbon hybrids enables superior energy storage performance. Matter. 2023;6(5):1604. https://doi.org/10.1016/j.matt.2023.03.013.

[28] Wang J, Shao YC, Ma YQ, Zhang D, Aziz S, Li ZJ, Woo HJ, Subramaniam R, Wang B. Facilitating rapid Na^+ storage through MoWSe/C heterostructure construction and synergistic electrolyte matching strategy. ACS Nano. 2024;18:10230.

[29] Wen DF, Zhang HY, Lin ZH, Yang CS, Wan BS, Gao H, Li SK, Zhang SS, Wang Y. WSe_2/$CoSe_2$ nanocrystals in situ growth on three-dimensional carbon nanofibers as anode material for long-life and high-rate sodium-ion batteries. J Alloy Compd. 2023;937:168417. https://doi.org/10.1016/j.jallcom.2022.168417.

[30] Yu J, Cao YD, Wang ML, Fan LL, Sun WG, Qi B, Zhang YX, Dong XY, Gao GG. Manipulation of the MoO_2/$MoSe_2$ heterointerface boosting high rate and durability for sodium/potassium storage. ACS Appl Mater Interfaces. 2022;14(32):36592. https://doi.org/10.1021/acsami.2c08080.

[31] Cui FY, Han MS, Zhou WY, Lai C, Chen YH, Su JW, Wang JS, Li HY, Hu YX. Superlattice-stabilized WSe_2 cathode for rechargeable aluminum batteries. Small Methods. 2022;6(12):2201281. https://doi.org/10.1002/smtd.202201281.

[32] He Y, Liu CL, Xie ZK, Xiao KT, Pai RZ, Chen G, Feng ZB, Kasai Y, Abudula A, Guan GQ. Construction of cobalt sulfide/molybdenum disulfide heterostructure as the anode material for sodium ion batteries. Adv Compos Hybrid Mater. 2023;6(3):85. https://doi.org/10.1007/s42114-023-00661-0.

[33] Kong HB, Cui W, Yan CS, Kong Y, Lv C, Chen G. Interface engineering on cobalt selenide composites enables superior Alkali-Ion storage. Chem Eng J. 2021;419:129490. https://doi.org/10.1016/j.cej.2021.129490.

[34] Ding YF, Cai JS, Sun YJ, Shi ZX, Yi YY, Liu BZ, Sun JY. Bimetallic selenide decorated nanoreactor synergizing confinement and electrocatalysis of Se species for 3D-printed high-loading K-Se batteries. ACS Nano. 2022;16(2):3373. https://doi.org/10.1021/acsnano.2c00256.

[35] Liu Y, Wan Q, Gong J, Liu ZW, Tao G, Zhao J, Chen L, Li WS, Wei XJ, Ni L, Song YZ. Confine, defect, and interface manipulation of Fe_3Se_4/3D graphene targeting fast and stable potassium-ion storage. Small. 2022;19(8):2206400. https://doi.org/10.1002/smll.202206400.

[36] Ge JM, Fan L, Wang J, Zhang QF, Liu ZM, Zhang EJ, Liu Q, Yu XZ, Lu BG. $MoSe_2$/N-doped carbon as anodes for potassium-ion batteries. Adv Energy Mater. 2018;8(29):1801477. https://doi.org/10.1002/aenm.201801477.

[37] Zhang SQ, Sun LL, Yu L, Zhai GH, Li LX, Liu XJ, Wang H. Core-shell $CoSe_2$/WSe_2 heterostructures@carbon in porous carbon nanosheets as advanced anode for sodium ion batteries. Small. 2021;17(49):2103005. https://doi.org/10.1002/smll.202103005.

[38] Wang XC, Zhao J, Chen Y, Zhu K, Ye K, Wang Q, Yan J, Cao DX, Wang GL, Miao CX. Molybdenum sulfide selenide ultrathin nanosheets anchored on carbon tubes for rapid-charging sodium/potassium-ion batteries. J Colloid Interf Sci. 2022;628:1041. https://doi.org/10.1016/j.jcis.2022.08.138.

[39] Hu RX, Sha DW, Cao X, Lu CJ, Wei YC, Pan L, Sun ZM. Anchoring metal-organic framework-derived ZnTe@C onto Elastic $Ti_3C_2T_x$ MXene with 0D/2D dual confinement for ultrastable potassium-ion storage. Adv Energy Mater. 2022;12(47):2203118. https://doi.org/10.1002/aenm.202203118.

[40] Jin JY, Park SK. Rational design of hierarchical Ni-Mo bimetallic Selenide/N-doped carbon microspheres toward high-performance potassium ion batteries. Appl Surf Sci. 2022;583:152491. https://doi.org/10.1016/j.apsusc.2022.152491.

[41] Lee JS, Park JS, Baek KW, Saroha R, Yang SH, Kang YC, Chou JS. Coral-like porous microspheres comprising polydopamine-derived N-doped C-coated $MoSe_2$ nanosheets composited with graphitic carbon as anodes for high-rate sodium-and potassium-ion batteries. Chem Eng J. 2023;456:141118. https://doi.org/10.1016/j.cej.2022.141118.

[42] Li CJ, Zhang YC, Yuan JX, Hu J, Dong HR, Li GF, Chen D, Li YN. Ultra-small few-layered $MoSe_2$ nanosheets encapsulated in nitrogen-doped porous carbon nanofibers to create large heterointerfaces for enhanced potassium-ion storage. Appl Surf Sci. 2022;601:154196. https://doi.org/10.1016/j.apsusc.2022.154196.

[43] Liu YR, Lei ZW, Liu RP, Li XY, Xiong PX, Luo YJ, Chen QH, Wei MD, Zeng LX, Qian QR. Sn-doped induced stable 1T-WSe_2 nanosheets entrenched on N-doped carbon with extraordinary half/full sodium/potassium storage performance. Rare Met. 2023;42(5):1557. https://doi.org/10.1007/s12598-022-02174-z.

[44] Hong G, Park SK. Co-MOF derived $MoSe_2$@$CoSe_2$/N-doped carbon nanorods as high-performance anode materials for potassium ion batteries. Int J Energ Res. 2022;46(8):10677. https://doi.org/10.1002/er.7866.

[45] Sun ZH, Wu XL, Xu JN, Qu DY, Zhao BL, Gu ZY, Li WH, Liang HJ, Gao LF, Fan YY, Zhou K, Han DX, Gan SY, Zhang YW, Niu L. Construction of bimetallic selenides encapsulated in nitrogen/sulfur Co-doped hollow carbon nanospheres for high-performance sodium/potassium-ion half/full batteries. Small. 2020;16(19):1907670. https://doi.org/10.1002/smll.201907670.

[46] Chen SF, Ma HL, Zhou XT, Jin D, Yan JF, Wang G, Zhao W, Yun JG, Zhang H, Zhang ZY, Chen RY. Heterostructure interface construction of cobalt/nickel diselenides hybridized with sp^2-sp^3 bonded carbon to boost internal/external sodium and potassium storage dynamics. ACS Appl Energy Mater. 2022;6(1):424. https://doi.org/10.1021/acsaem.2c03333.

[47] Zhang N, Chen XJ, Zhao JJ, He PF, Ding XL. Mass produced Sb/P@C composite nanospheres for advanced sodium-ions battery anodes. Electrochim Acta. 2023;439:141602. https://doi.org/10.1016/j.electacta.2022.141602.

[48] Wu H, Li S, Yu XB. Structural engineering of SnS quantum dots embedded in N, S, Co-doped carbon fiber network for ultrafast and ultrastable sodium/potassium-ion storage. J Colloid Interf Sci. 2024;653:267. https://doi.org/10.1016/j.jcis.2023.09.044.

[49] Dong GS, Yu HY, Li LX, Zhang RY, Yang X, Zhu K, Wang GL, Cao DX. Surface engineering of core-shell MoS_2@N-doped carbon spheres as stable and ultra-long lifetime anode for sodium-ion batteries. J Colloid Interf Sci. 2023;647:395. https://doi.org/10.1016/j.jcis.2023.05.075.

[50] Tu JW, Tong HG, Wang PC, Wang DD, Yang Y, Meng XF, Hu L, Wang H, Chen QW. Octahedral/tetrahedral vacancies in Fe_3O_4 as K-storage sites: a case of anti-spinel structure material serving as high-performance anodes for PIBs. Small. 2023; 19(34):2301606. https://doi.org/10.1002/smll.202301606.

[51] Zheng H, Wang JY, Li HW, Deng SQ, Zuo YZ, Yan W, Zhang JJ. Constructing a novel heterostructure of $NiSe_2/CoSe_2$ nanoparticles with boosted sodium storage properties for sodium-ion batteries. J Mater Chem A. 2022;10(30):16268. https://doi.org/10.1039/d2ta04237a.

[52] Cheng JY, Niu ZL, Zhao ZP, Pei XD, Zhang S, Wang HQ, Li D, Guo ZP. Enhanced ion/electron migration and sodium storage driven by different MoS_2-$ZnIn_2S_4$ heterointerfaces. Adv Energy Mater. 2022;13(5):2203248. https://doi.org/10.1002/aenm.202203248.

[53] Li SK, Zhang HY, Cao YL, Zhang SS, Liu ZJ, Yang CS, Wang Y, Wan BS. Self-assembled nanoflower-like $FeSe_2/MoSe_2$ heterojunction anode with enhanced kinetics for superior-performance Na-ion half/full batteries. Nanoscale. 2023;15(12): 5655. https://doi.org/10.1039/d2nr06672f.